Effects of shear, defocus, and wavefront error on the theoretical performance of the composite infrared spectrometer for Cassini

Anthony J. Martino[a] and John G. Hagopian[b]

[a]Laser/Electro-Optics Branch, Code 554, NASA Goddard Space Flight Center, Greenbelt, MD 20771
[b]Optics Branch, Code 551, NASA Goddard Space Flight Center, Greenbelt, MD 20771

ABSTRACT

The combined effects on performance of shear between the two arms, defocus of the detector, and difference in wavefront between the two arms of a Fourier transform spectrometer using cube corner retroreflectors were investigated. Performance was characterized by the amplitude of the fringe signals coming from a detector as the path-length difference was scanned. A closed-form expression was found for the combined effects of shear and defocus, and it was found that defocus had no effect in the absence of shear. The effect of wavefront error was modeled numerically and assumed to be independent of shear and defocus. Results were compared with measurements made on the breadboard and engineering model of the Composite Infrared Spectrometer for the Cassini mission to Saturn, and good agreement was found.

Keywords: Cassini, CIRS, Michelson interferometer, Fourier transform spectrometer, reflectance, shear, defocus, wavefront, alignment, modulation

1. INTRODUCTION

The Composite Infrared Spectrometer[1,2] (CIRS) for the Cassini mission to Saturn is a Fourier transform infrared spectrometer that contains three Michelson-type interferometers. One is used for spectral measurements in the mid-infrared (MIR) band of 7 to 17 μm; another is used in the far-infrared (FIR) band of 17 to 1000 μm. The moving elements of these two interferometers are mounted on a common scan mechanism[3]. The third is a reference interferometer[4] that measures the position of the scan mechanism.

During the development of the MIR interferometer, it became necessary to determine the theoretical performance of the real, as opposed to ideal, interferometer. Effects of all known departures from ideal were to be calculated and compared with the measured performance of the actual hardware. Effects that were included in the calculations were reflectances of all surfaces in the beamsplitter/compensator stack, wavefront aberrations due to the figures of these surfaces and the retroreflectors, and two forms of misalignment: shear and defocus. Performance of the interferometer was measured in terms of the observed modulation of the output signal.

2. CONCEPTS AND DEFINITIONS

A conceptual sketch of the MIR interferometer is shown in Figure 1. A source is nominally located at the focal plane of the input lens. An image is formed, nominally at the focal plane of the output lens. A detector, the area of which defines the field of view, is also located nominally at the output focal plane. In the subsequent analysis, defocus will refer to axial displacement of the source or detector from the input or output focal plane.

At the center of the interferometer is a beamsplitter/compensator pair. The substrate material is potassium bromide (KBr). The beamsplitter coating, which is deposited on the second surface of the beamsplitter, is nominally 50% reflective and 50% transmissive for both polarizations across the spectral bandwidth of interest.

The beams transmitted and reflected from the beamsplitter surface propagate to a pair of cube-corner retroreflectors. These retroreflectors terminate the arms of the Michelson interferometer. The beams that return from the retroreflectors are recombined at the beamsplitter, then focused by the output lens onto the detector. As the moving retroreflector translates along the optical axis, the path length difference between the two arms changes. This gives rise to a varying signal recorded by the detector. This signal can be characterized by its modulation, given by

$$M = \frac{S_{max} - S_{min}}{S_{max} + S_{min}} \quad , \tag{1}$$

where S is the signal recorded by the detector.

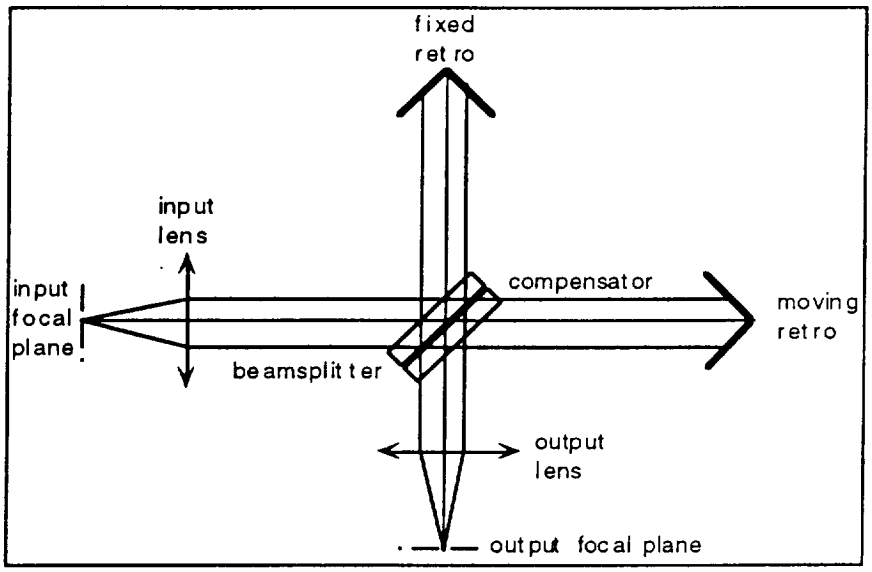

Figure 1. Conceptual sketch of the MIR interferometer.

The actual reflectance of the beamsplitter surface deviates from ideal performance. Also, there is no antireflection coating on the first surface of the beamsplitter or either surface of the compensator. The reflectance of uncoated KBr at the relevant angle of incidence (37°) is high enough that a significant amount of light goes into stray beams that are reflected at surfaces other than the nominal beamsplitter surface. These surfaces are slightly tilted with respect to the beamsplitter surface, so the stray beams do not contribute to the modulation of the interferogram recorded at the detector. However, they do contribute an offset term.

Nominally, the apexes of the cube corners are located on the optical axis, which is defined by the focal point and center of the input lens. In this case, rays in the fixed and moving arms that come from a single ray incident on the beamsplitter meet again when the beams are recombined.

If one or both of the cube corners is displaced laterally from its nominal position, the rays returning from the two arms are displaced. This displacement of the two returning beams is called shear. Alone, and in combination with defocus, it affects the modulation of the detected signal.

Errors in the surface figures of the beamsplitter, compensator, and retroreflectors cause a variation of phase difference across the aperture of the interferometer. This also contributes to a loss of modulation.

Except for shear and defocus, these effects are, to a good approximation, independent of each other. Consequently, they can be treated separately and then combined to yield a final result.

3. SURFACE REFLECTANCE

It is well known[5] that, for an ideal Michelson interferometer, the modulation is given by

$$M = 4RT \quad , \tag{2}$$

where R is the reflectance and T is the transmittance of the beamsplitter. When there are additional reflective surfaces associated with the beamsplitter, additional stray beams are created that contribute to the total power received by the detector but not to the interferogram.

The zero order beam of the interferometer consists of rays that split and recombine at the beamsplitter surfaces, and do not reflect at any other beamsplitter or compensator surface. The zero order power that reaches the detector (the main beam) from the moving and fixed arms is given by

$$P_{mm} = P_{in} T_{ue}^{3} T_{ui}^{2} R_{ci} T_{ci}$$

$$P_{mf} = P_{in} T_{ue}^{4} T_{ui}^{3} R_{ce} T_{ci} \quad (3)$$

where P_{in} is the input power; the subscripts "c" and "u" mean "coated" and "uncoated" with the beamsplitter coating; and "i" and "e" mean internal and external reflection. Then the amplitude of the fringes is

$$A = 2\sqrt{P_{mf} P_{mm}} = 2\sqrt{T_{ue}^{7} T_{ui}^{5} R_{ce} T_{ci} R_{ci} T_{ci}} \quad . \quad (4)$$

A similar expression can be found for zero order power that is returned to the source. In the MIR interferometer, the fraction of the input power that reaches the detector in a zero-order beam varies between 11% and 37%, depending on wavelength and polarization. This leads to modulation of the main beam that varies between 89% and 97%. The complementary main beam, which returns to the source, accounts for another 32% to 78% of the input power.

Stray beams can be classified as first order, second order, etc., based on the number of reflections made at the front beamsplitter surface and the compensator surfaces. Together, these higher-order beams account for 10% to 35% of the input power. If we (very roughly) approximate that the higher-order power is split between the detector and the source according to the same ratio as for the zero-order power, and calculate modulation as

$$M = \frac{A}{P_{out}} \quad , \quad (5)$$

where P_{out} is the mean power reaching the detector from all beams, we obtain the results shown in Figure 2.

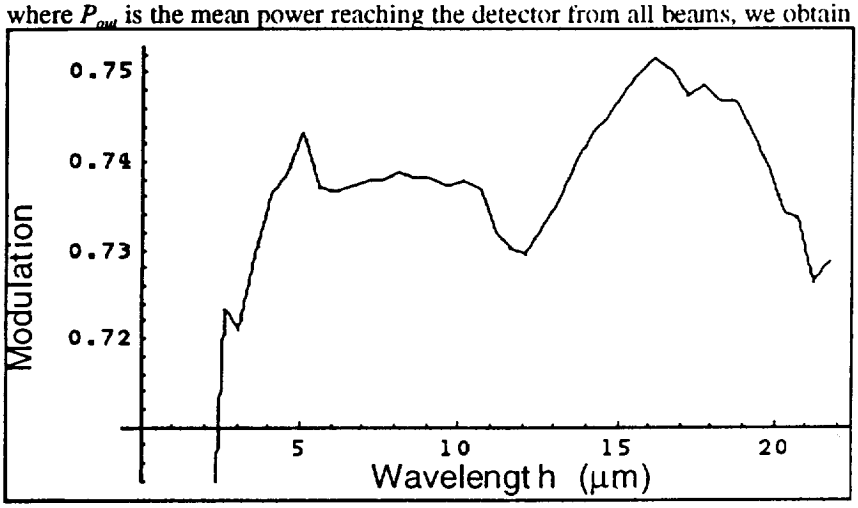

Figure 2. Modulation of the output light due to beamsplitter and compensator surface reflectance, averaged between *s* and *p* polarizations.

4. WAVEFRONT ERROR

The electric field at a point (x,y) in the aperture, assuming equal powers in the two arms, is

$$\mathbf{E}(x, y) = \frac{1}{2} \mathbf{E}_0 \left[e^{i\phi_1(x,y)} + e^{i(\phi_1(x,y) + kz + \Delta\phi_e(x,y))} \right] \quad (6)$$

where ϕ_1 is the phase at (x,y) from one interferometer arm in radians, $\Delta\phi_e$ is the phase difference between the two arms due to wavefront errors , and z is the mean path length difference.

The power at the interference plane is

$$P(x, y) = E(x, y)E^*(x, y)$$
$$= \frac{1}{2} E_0^2 \left[1 + \cos\left(kz + \Delta\phi_e(x, y)\right)\right]$$
$$= P_0 \left[1 + \cos\left(kz + \Delta\phi_e(x, y)\right)\right] \quad (7)$$

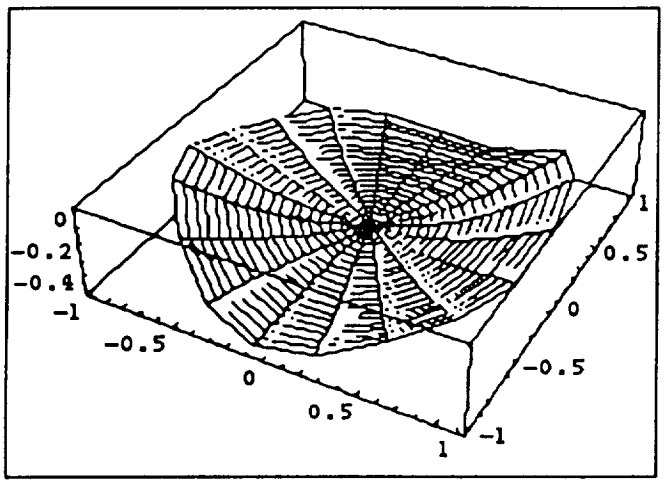

Figure 3. Phase difference in waves (at 9.1 μm) between the fixed and moving arms of the CIRS MIR interferometer due to surface figures. Horizontal units are fractions of pupil radius.

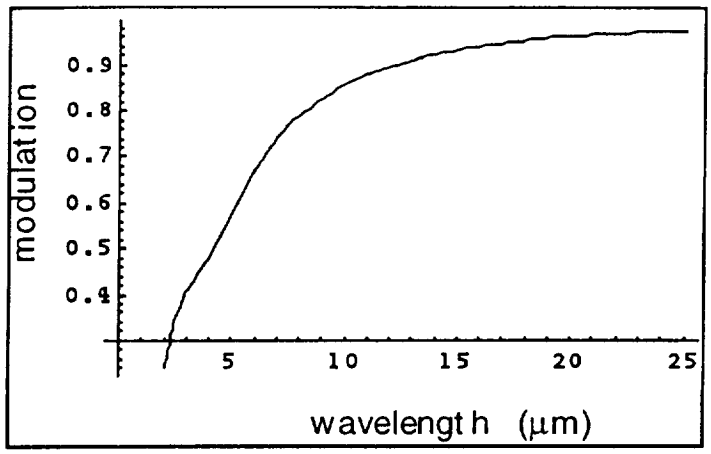

Figure 4. Modulation of the CIRS MIR interferometer due to the wavefront difference shown in Figure 3.

The interferogram is produced by focusing the total power in the aperture to a spot, then capturing the spot on a detector:

$$I(z) = \int_A P_0 \left[1 + \cos\left(kz + \Delta\phi_e(x, y)\right)\right] dxdy$$
$$= P_0 A + P_0 \int_A \cos\left(kz + \Delta\phi_e(x, y)\right) dxdy$$
$$= P_0 A + P_0 \cos kz \int_A \cos \Delta\phi_e(x, y) dxdy - P_0 \sin kz \int_A \sin \Delta\phi_e(x, y) dxdy \quad (8)$$

Let

$$H_1 = \int_A \cos \Delta\phi_e(x, y) dxdy$$
$$H_2 = \int_A \sin \Delta\phi_e(x, y) dxdy \quad (9)$$

Then

$$I(z) = AP_0 + P_0 H_1 \cos kz - P_0 H_2 \sin kz$$
$$= AP_0 + P_0 \sqrt{H_1^2 + H_2^2} \left(\cos(kz + \Phi)\right) \quad (10)$$

where $\tan \Phi = \frac{H_2}{H_1}$. Then the mean of the interferogram is AP_0 and the modulation is

$$M = \frac{\sqrt{H_1^2 + H_2^2}}{A} \tag{11}$$

For some wavefront shapes, H_1 and H_2 could be calculated analytically. In practice, it is necessary to compute them numerically from measured data. To model the CIRS MIR interferometer, surface figures or wavefront distortions were measured for each component using a Zygo interferometer. Wavefronts from the fixed and moving arms, and wavefront difference, were computed using these measured data. Figure 3 is a plot of computed wavefront difference at 7.1 μm wavelength, and Figure 4 is a plot of the resulting modulation as a function of wavenumber.

5. SHEAR AND DEFOCUS

A treatment of the effect of shear in a cube-corner Michelson interferometer has been published by Murty[6]. For a cube-corner Michelson interferometer with a circular field of view, no defocus, at zero path difference, the modulation is given by

$$M = \frac{J_1(2\sigma s\sqrt{\pi\Omega})}{\sigma s\sqrt{\pi\Omega}} \tag{12}$$

where σ is the wavenumber, s is the wavefront shear (twice the cube corner displacement), and Ω is the solid angle subtended by the field of view. Kauppinen and Saarinen[7] have extended this theory to predict line shape distortions in the spectral domain.

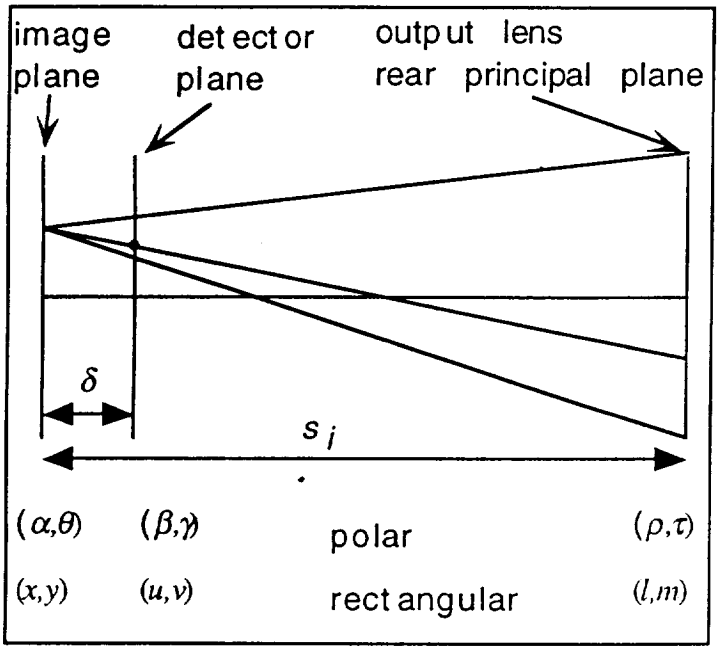

Figure 5. Geometry for defocus/shear theory, showing significant planes and polar and rectangular coordinates used therein.

Saarinen and Kauppinen[8] have examined the effect of a defocused point source on the interferogram and in the spectral domain, expanding on work by Guelachvili[9]. Kunz and Goorvitch[10] have examined the combined effects of source defocus and mirror misalignment in a Michelson interferometer that uses plane mirrors. Here we present a treatment of the combined effects of defocus and shear on the modulation at ZPD of a cube-corner Michelson interferometer looking at an object that fills a small but nonzero field of view.

The geometry is shown in Figure 5. Each point in the source (not shown) is imaged to a point in the image plane (nominally the focal plane of the output lens) at a distance s_i from the rear principal plane of the output lens. A planar detector is located at some distance δ from the image plane. For each point (u,v) in the detector plane and (l,m) in the pupil, there is a corresponding point (x,y) in the image plane.

The pupil of the optical system is circular, with radius R_p. In general, the source is not at the focal plane of the input lens, so the wavefront incident on the output lens is spherical with radius R_w. In this analysis, R_w is assumed to be much greater than the maximum path length difference between the two arms of the interferometer, so the wavefronts from the two arms can be treated as having the same radius of curvature.

Consider a point on the y-axis in the image plane. The wavefront that is focused onto it is described paraxially in the pupil plane as

$$z(l, m) = m\frac{y}{s_i} + \frac{l^2 + m^2/(1 - (y/s_i)^2)}{2R_w} \tag{13}$$

A wavefront that is sheared with respect to this one by s is

$$z(l, m) = (m + s)\frac{y}{s_i} + \frac{l^2 + (m + s)^2/(1 - (y/s_i)^2)}{2R_w} \tag{14}$$

Then the phase difference between the two waves is

$$\Delta\Phi(0, y, l, m) = \frac{2\pi}{\lambda}\left(s\frac{y}{s_i} + \frac{2sm + s^2}{2R_w(1 - (y/s_i)^2)}\right) \tag{15}$$

Since the image height is much smaller than the image distance, we can eliminate terms of order 2 or higher in y/s_i, yielding

$$\Delta\Phi(0, y, l, m) = \frac{2\pi}{\lambda}\left(s\frac{y}{s_i} + \frac{2sm + s^2}{2R_w}\right) \quad . \tag{16}$$

It can be shown that for arbitrary field points, under the same conditions, the same result holds. Then

$$P(x, y, l, m, z) = P_0 + P_0 \cos k\left(z + \frac{ys}{s_i} + \frac{s^2}{2R_w} + \frac{sm}{R_w}\right) \tag{17}$$

The power that strikes a point (u,v) on the detector is

$$P(u, v, z) = \int_0^{\infty} \rho d\rho \int_0^{2\pi} d\tau P(\alpha, \theta, \rho, \tau) \quad , \tag{18}$$

where (u,v), (α,θ), and (ρ,τ) are all collinear. Substituting (17) into (18) and using some geometry to express image plane coordinates in terms of pupil and detector plane coordinates, we obtain

$$P(u, v, z) = \pi R_p^2 P_0 + P_0 \int_0^{\infty} \rho d\rho \int_0^{2\pi} d\tau \cos k\left[\begin{array}{l} z + \left(\frac{s}{R_w} - \frac{s\delta}{s_i(s_i - \delta)}\right)\rho \sin \tau \\ + \frac{s\delta v}{s_i(s_i - \delta)} + \frac{sv}{s_i} + \frac{s^2}{2R_w} \end{array}\right] , \tag{19}$$

which evaluates to

$$P(u, v, z) = \pi R_p^2 P_0 + \frac{2\pi P_0 R_p}{k\left[\frac{s}{R_w} - \frac{s\delta}{s_i(s_i - \delta)}\right]} J_1\left(kR_p\left[\frac{s}{R_w} - \frac{s\delta}{s_i(s_i - \delta)}\right]\right) \cos\left(k\left[\frac{sv}{s_i - \delta} + \frac{s^2}{2R_w} + z\right]\right) . \tag{20}$$

In the case of a rectangular detector with dimensions Δu and Δv, the power integrated across the detector is

$$P(z) = \pi R_p^{\,2} P_0 \Delta u \Delta v$$

$$+2\pi P_0 R_p^{\,2} \Delta u \frac{J_1(\Psi_1)}{\Psi_1} \frac{s_i - \delta}{ks} \left[\left(\sin \frac{ksv_{max}}{s_i - \delta} - \sin \frac{ksv_{min}}{s_i - \delta} \right) \cos k\left[\frac{s^2}{2R_w} + z \right] + \left(\cos \frac{ksv_{max}}{s_i - \delta} - \cos \frac{ksv_{min}}{s_i - \delta} \right) \sin k\left[\frac{s^2}{2R_w} + z \right] \right], \quad (21)$$

where

$$\Psi_1 = kR_p \left[\frac{s}{R_w} - \frac{s\delta}{s_i(s_i - \delta)} \right] . \quad (22)$$

Then the modulation is

$$M(s, \delta, \Delta v) = 2 \frac{J_1(\Psi_1)}{\Psi_1} \frac{\sin(\Psi_2)}{\Psi_2} , \quad (23)$$

where

$$\Psi_2 = \frac{ks\Delta v}{2(s_i - \delta)} . \quad (24)$$

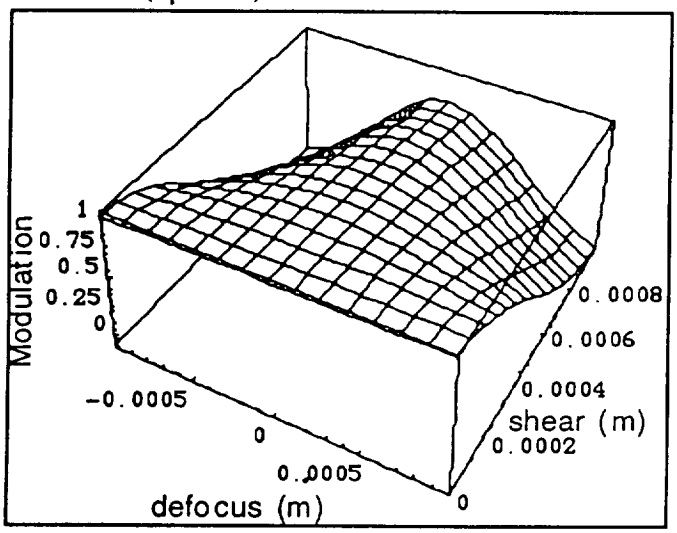

Figure 6. Effect of shear and defocus on modulation of the CIRS MIR interferometer at 10 μm wavelength.

An interesting feature of this result is that, while shear affects the modulation by itself, defocus at the output affects modulation only in the presence of shear. With shear present, modulation is maximized by placing the detector not at the focal plane of the output lens, but at the image of the source. (The image of the source coincides with the focal plane of the output lens if there is no defocus at the input.)

Figure 6 illustrates the effect of shear and output defocus on the modulation of the CIRS MIR interferometer. The detector in this instance is an array of pixels, each of which can be regarded as a 200 μm square.

6. COMPARISON OF THE COMBINED EFFECTS WITH EXPERIMENT

All of these effects were combined to produce predictions of the performance of the CIRS MIR interferometer. The predictions were compared with measurements made on the engineering and flight models of the instrument. The details of the experimental measurements are described in another paper[11].

In Figure 7, we show predictions of measured spectra using a 500° C blackbody source under various conditions. The calculations include the effects described above and the relative spectral responsivity of a HgCdTe detector. Figure 8 is an example of actual data measured under corresponding conditions in a CIRS breadboard, using a detector similar but not identical to the one whose responsivity was used in the calculation.

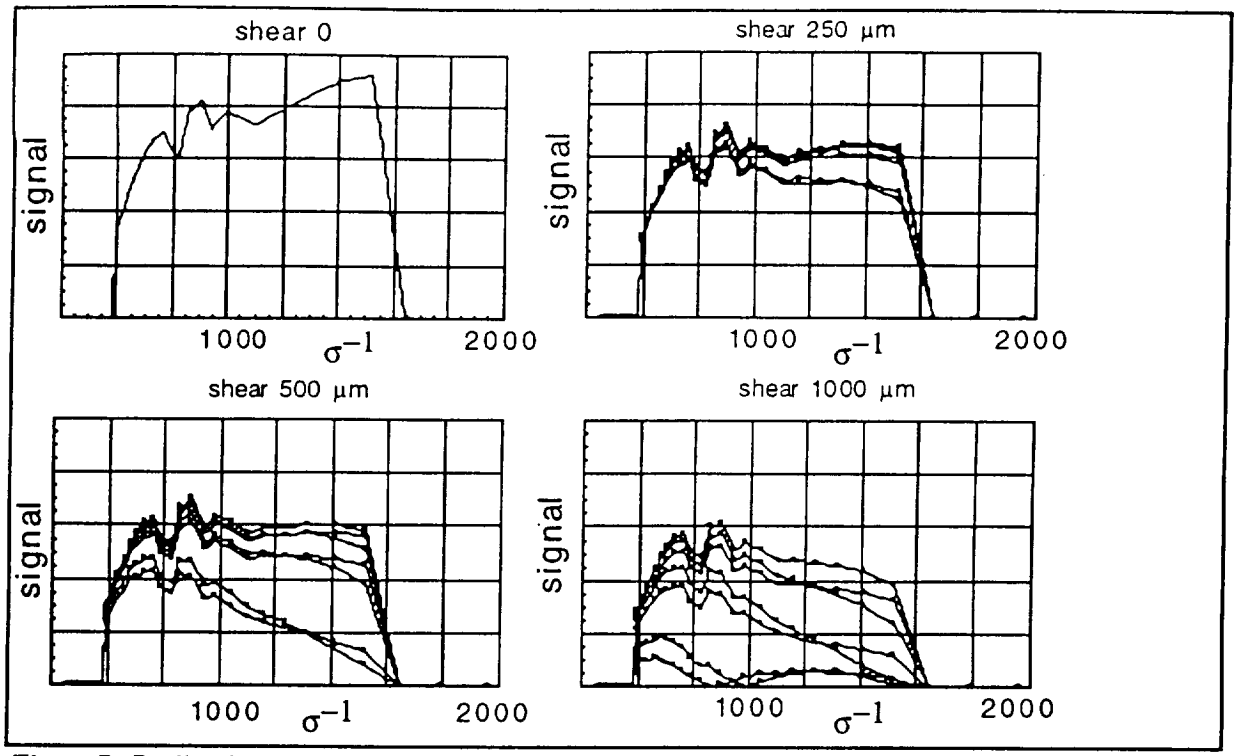

Figure 7. Predicted performance of the CIRS MIR interferometer measuring a 773 K blackbody spectrum. Effects of beamsplitter/compensator reflectance, surface figures, shear, output defocus, and detector responsivity are included. Each plot shows detector response in arbitrary units as a function of wavenumber with defocus (from top) 0, ±250 μm, ±500 μm, and ±1000 μm.

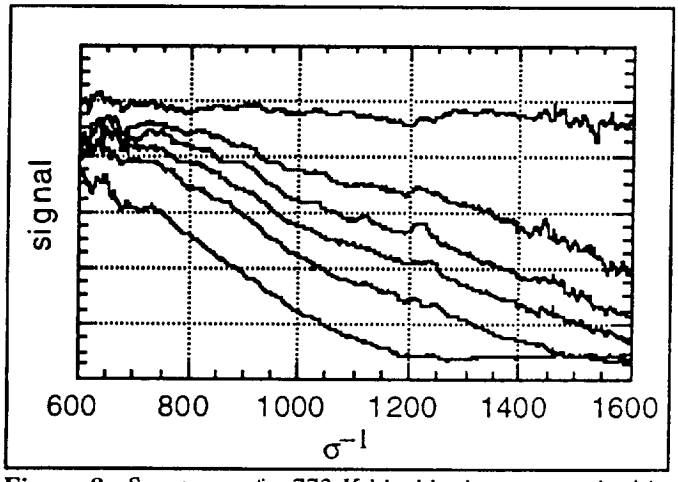

Figure 8. Spectrum of a 773 K blackbody, measured with (from top) 200 μm shear and no defocus, 1000 μm of shear and 0, 200 μm, 300 μm, 400 μm, and 600 μm of output defocus.

With no shear, the theoretical plot is simply the blackbody spectrum multiplied by the relative responsivity of the detector. In the absence of defocus, the effect of shear is noticeable but mild, being most pronounced at higher wavenumbers (shorter wavelengths).

As shear is increased, the effects of defocus become more and more pronounced. Large degradations appear first at higher wavenumbers, then propagate to lower wavenumbers as the shear or defocus increases. Note that there is little difference between the effects of positive and negative defocus.

The experimental results agree well with the theory. As expected, 200 μm of shear with no defocus shows a nearly flat spectrum. With 1000 μm of shear, the performance at higher wavenumbers is degraded markedly even with no defocus. Performance at the lower wavenumbers is still affected only slightly. As defocus increases, performance drops quickly at high wavenumbers and more slowly at low wavenumbers. At the largest defocus (1000 μm), the performance actually recovers slightly at the highest wavenumbers.

The theory presented in this paper was used in the diagnosis and characterization of the CIRS instrument. With this information, it was possible to determine that after alignment of all the optics, the instrument performance was as good as could be obtained with the fabricated hardware.

7. REFERENCES

1. V. Kunde *et. al.*, "Cassini infrared Fourier spectroscopic investigation," *Proc. SPIE* **2803**, pp. 162-177, 1996.
2. P. W. Maymon *et al.*, "Optical design of the composite infrared spectrometer (CIRS) for the Cassini mission," *Proc. SPIE* **1945**, pp. 100-111, 1993.
3. C. F. Hakun and K. A. Blumenstock, "A cryogenic scan mechanism for use in Fourier transform spectrometers," in *NASA Johnson Space Flight Center 29th Aerospace Mechanisms Symposium*, pp. 316-333, 1995.
4. A. J. Martino and D. M. Cornwell, "Reference interferometer using a semiconductor laser/LED reference source in a cryogenic Fourier-transform spectrometer," *Proc. SPIE* **3435**, in press, 1998.
5. R.J. Bell, *Introductory Fourier Transform Spectroscopy*, p. 112, Academic Press, New York, 1972.
6. M. V. R. K. Murty, "Some more aspects of the Michelson interferometer with cube corners," *J. Opt. Soc. Am.* **50**, pp. 7-10, 1960.
7. J. Kauppinen and P. Saarinen, "Line-shape distortions in misaligned cube corner interferometers," *Appl. Opt.* **31**, pp. 69-74, 1992.
8. P. Saarinen and J. Kauppinen, "Spectral line-shape distortions in Michelson interferometers due to off-focus radiation source," *Appl. Opt.* **31**, pp. 2353-2359, 1992.
9. G. Guelachvili, "Distortions in Fourier spectra and diagnosis," *Spectrometric Techniques*, G. Vanasse, V. II, pp. 1-62, Academic Press, New York, 1981.
10. L. W. Kunz and D. Goorvitch, "Combined effects of a converging beam of light and mirror misalignment in Michelson interferometry," *Appl. Opt.* **13**, pp. 1077-1079, 1974.
11. J. G. Hagopian *et. al*, "Shear/defocus sensitivity of the mid-infrared channel (MIR) of the composite infrared spectrometer (CIRS) for the Cassini mission to Saturn," *Proc. SPIE* **3435**, in press, 1998.